

CoreNet: Conflict Resolution Network for Point-Pixel Misalignment and Sub-Task Suppression of 3D LiDAR-Camera Object Detection*

Yiheng Li^{a,b}, Yang Yang^{a,b,*}, Zhen Lei^{a,b,c}

^a *State Key Laboratory of Multimodal Artificial Intelligence Systems (MAIS), Institute of Automation, Chinese Academy of Sciences, Beijing, 100190, China*

^b *School of Artificial Intelligence, University of Chinese Academy of Sciences, Beijing, 100049, China*

^c *Centre for Artificial Intelligence and Robotics, Hong Kong Institute of Science & Innovation, Chinese Academy of Sciences, Hongkong, 999077, China*

Abstract

Fusing multi-modality inputs from different sensors is an effective way to improve the performance of 3D object detection. However, current methods overlook two important conflicts: point-pixel misalignment and sub-task suppression. The former means a pixel feature from the opaque object is projected to multiple point features of the same ray in the world space, and the latter means the classification prediction and bounding box regression may cause mutual suppression. In this paper, we propose a novel method named **Conflict Resolution Network** (CoreNet) to address the aforementioned issues. Specifically, we first propose a dual-stream transformation module to tackle point-pixel misalignment. It consists of ray-based and point-based 2D-to-BEV transformations. Both of them achieve approximately unique mapping from the image space to the world space. Moreover, we introduce a task-specific predictor to tackle sub-task suppression. It uses the dual-branch structure which adopts class-specific query and Bbox-specific query to corresponding sub-tasks. Each task-specific query is constructed of task-specific feature and general feature, which allows the heads to adaptively

*Yiheng Li and Yang Yang contribute equally to this work.

*Corresponding author

Email addresses: liyiheng2024@ia.ac.cn (Yiheng Li), yang.yang@nlpr.ia.ac.cn (Yang Yang), zhen.lei@ia.ac.cn (Zhen Lei)

select information of interest based on different sub-tasks. Experiments on the large-scale nuScenes dataset demonstrate the superiority of our proposed CoreNet, by achieving 75.6% NDS and 73.3% mAP on the nuScenes test set without test-time augmentation and model ensemble techniques. The ample ablation study also demonstrates the effectiveness of each component. The code is released on <https://github.com/liyih/CoreNet>.

Keywords: multi-modality, 3D object detection, point-pixel misalignment, sub-task suppression

1. Introduction

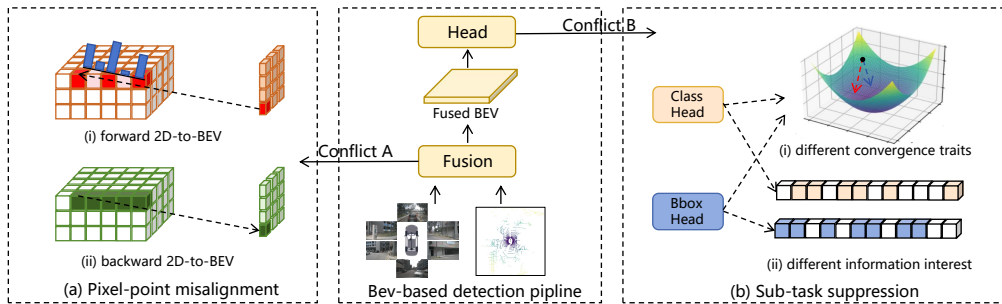


Figure 1: Display of two conflicts for 3D LiDAR-camera object detection. The schematic diagram of point-pixel alignment is provided on the left, while the schematic diagram of sub-task suppression is shown on the right.

3D object detection is to predict the locations, sizes, categories, orientations, and velocities of 3D objects around the ego vehicle, which plays a critical role in autonomous driving and robotics [1–3]. High-quality object detection results can be used as reliable observations for downstream tasks such as object tracking and path planning [4, 5]. In recent years, multi-modality 3D object detection has received more and more attention due to its robustness and high performance [6–9]. Camera and LiDAR are the two most common sensors. The former can provide rich semantic information, the latter can capture the precise structure of the objects. Compared to traditional single-modality 3D object detection, the application of multiple sensors can often achieve superior and more robust results. This is because multiple modalities have rich information representation capability and complement each other [5, 10–13].

As the inputs from different modalities have heterogeneous data representations, most existing methods [14, 15] first project different modalities into a unified space e.g. the bird’s eye view (BEV), and then perform the fusion process. However, they often overlook two important conflicts, i.e., point-pixel misalignment and sub-task suppression (as shown in Fig. 1). Point-pixel misalignment appears in the 2D-to-BEV transformation stage. The current 2D-to-BEV transformation is divided into forward [16] and backward [17] methods. Both of them project a pixel feature from an opaque object to multiple points of the pixel-object ray which connects the object and the pixel feature in the camera system. In reality, each pixel feature of opacity objects should be uniquely projected or mostly concentrated to a single point in the pixel-object ray. The forward methods first predict the distribution probability among the uniformly sampled points of the ray from a pixel. Then, they scatter the pixel feature to the sampled points based on the distribution probability. Due to the fact that the probability is not a one-hot distribution, a pixel feature will be projected to multiple points of the same pixel-object ray. For backward methods, each point in the world space will be aligned with the corresponding pixel via the camera parameter. In this way, a pixel feature will be scattered to all the sampled points of the same pixel-object ray. Sub-tasks suppression appears in the prediction stage. The task of 3D object detection can be divided into two sub-tasks: classification prediction and bounding box (Bbox) regression. They are supervised with different kinds of functions, e.g., classification often relies on cross entropy loss and bounding box regression uses L1 Loss. These two sub-tasks may have different convergence directions and speeds, causing mutual suppression between sub-tasks during the joint training. In addition, different information of interest between sub-tasks will also give rise to the sub-tasks suppression [18]. Thus, how to address the problems of point-pixel misalignment and sub-task suppression have always been the core concerns.

In this paper, we propose a novel LiDAR-camera **Conflict Resolution Network** (CoreNet) to tackle the mentioned conflicts. For one thing, we introduce dual-stream transformation to overcome the point-pixel misalignment. It consists of ray-based and point-based 2D-to-BEV transformations. For the ray-based branch, inspired by BEVDepth [19], we adopt the one-hot distribution to supervise the scattered probability along each pixel-object ray. It will guarantee a pixel feature is mostly concentrated to a single point in the pixel-object ray. For the point-based branch, we adopt the point cloud from LiDAR as the guidance. LiDAR point clouds mainly distribute on the

surface of the opaque objects, and the occlusion relationship between the captured objects is basically the same as that of multi-view cameras. Based on this characteristic, each ray emitted by LiDAR will only return a unique landing signal to the sensor (located on opaque obstacles or backgrounds). We divide the point clouds into several bins, and each point of the same bin is located in the same BEV grid. The points in the same bin are projected to the image space. Corresponding pixel features are considered as their features which are pooled to be the BEV grid feature. For another, we propose a task-specific predictor to tackle the sub-task suppression. Most 3D object detections typically use separate prediction heads to extract sub-task features from the same feature [14, 20, 21]. The concerns of different heads are different during feature extraction, which may reduce the sub-task suppression in the supervision and prediction. However, such a strategy of eliminating the suppression between sub-tasks is implicit and uncontrollable. Some methods [22, 23] adopt the decoupling strategy which uses different features for classification and regression learning. Suppression mainly comes from different supervised signals, but there may be still some correlations between different sub-tasks. For example, the size and velocity of an object can reflect its type to an extent. Although the influence of supervised signals can be reduced by using fully separate features as previous decoupling manners, this may lead to difficulty in learning the relationship between classification and regression. In contrast, we extract general and specific features. General features are able to capture the correlations of sub-tasks and are used for both classification and regression, while specific features contain the information that is preferred by a certain sub-task and is used for a specific prediction head. Specifically, We first explicitly construct features with different task preferences, and task-specific supervision is introduced to make this process more controllable. Then, the general feature is extracted for both prediction heads. After that, a task-specific fuser combines the task-specific and general features to obtain the task-specific query, which adaptively selects information of interest. Finally, the task-specific query is inputted to the corresponding sub-task head.

Our proposed CoreNet achieves superior performance on the large-scale nuScenes [24] dataset by achieving 75.6% NDS and 73.3% mAP on the nuScenes test set. It also beats the latest state-of-the-art approaches (i.e., IS-Fusion [15] and DAL [25]) on both nuScenes test and val set. Ablation experiments demonstrate the effectiveness of our proposed dual-stream transformation and task-specific predictor. The main contributions are as follows:

(1) We propose a novel multi-modality 3D object detection framework named CoreNet, which focuses on tackling the conflicts in the fusion and prediction stages. (2) We design the dual-stream transformation and task-specific predictor to solve the point-pixel misalignment and to solve the sub-task suppression, respectively. (3) We confirm the efficacy of the proposed CoreNet framework for LiDAR-camera 3D object detection by achieving superior performance on large-scale nuScenes dataset.

2. Related Work

2.1. Camera-Based 3D object detection

Camera-based 3D object detection is a fast and low economic cost solution in autonomous driving. Typically, it can be categorized into monocular and multi-view methods. For monocular detection, researchers directly attach prediction heads to 2D image backbone [26, 27]. Depth estimation sometimes accompanies these methods [28]. For multi-view detection which has higher accuracy and stronger perception capability, it can be divided into BEV-based [17, 19, 21, 29] and DETR-based methods [30–32]. The former first extracts bird’s-eye-view (BEV) features based on image features through view transformation. View transformation can be categorized into forward [16] and backward [17] transformations. Then, 3D objects are predicted based on the BEV features. The latter firstly interacts with the object queries with the image tokens through attention mechanism[33, 34], and then predicts the 3D objects based on the transformer outputs. Some methods combine both forward and backward transformations. For example, FB-BEV [35] proposes a Depth-Aware Backward Projection to enhance the depth consistency between forward and backward transformations, thus obtaining high-quality BEV representations.

2.2. LiDAR-Based 3D object detection

LiDAR-based 3D object detection can predict reliable results from the captured 3D structural information. Current LiDAR-based 3D object detection can be divided into point-based [36–40] and transformation-based [26, 41–47] methods. Point-based methods directly extract features from raw point clouds and predict objects based on point-level features. The main challenge of these methods is the irregular format of the point cloud. Researchers construct many network structures, such as PointNet [37], to solve this problem. Transformation-based methods usually transform the

original point clouds into a regular format, such as voxels [41–44] and pillars [26, 45, 46]. After that, the 3D bounding box is predicted based on the transformed inputs. The main advantage of these methods is that they can use flexible and mature standard convolutional networks [46] or sparse 3D convolutional networks [44] to process features. However, the transformation process of data format may lead to information loss.

2.3. LiDAR-Camera 3D object detection

Mutli-modality 3D object detection uses camera and LiDAR sensors to capture texture and geometry information, respectively. Thus, it achieves more robust and higher performance than uni-modality 3D object detection, i.e., camera-based or LiDAR-based approach. How to efficiently fuse heterogeneous data is the key point for multi-modality 3D object detection [48–50]. Early works often use the LiDAR branch as the leading role for prediction, with camera inputs only serving as a way to supplement information. Point-painting [51] uses the segmentation masks of the images as a new feature dimension for the point cloud. MVP [52] uses the images to generate virtual points to complement the LiDAR point clouds, which can give objects a more complete contour. Transfusion [20] first predicts the results by the LiDAR branch and then refines the outputs based on the image inputs. The effectiveness of these methods is overly dependent on the LiDAR branch. When there are problems with the LiDAR branch, this type of method will not be able to achieve correct results. In view of this, the subsequent works equally emphasize both modalities.

Recently, researchers have begun to focus on finding a feature-level fusion, which can fully extract and integrate information from different modalities. MVX-Net [53] proposes pointfusion and voxelfusion strategies to make better interactions. The former is an early-stage fusion, while the latter is a late-stage fusion. To improve the robustness of feature fusion in difficult scenarios, Autoalignv2 [54] proposes cross-modality attention with soft correspondence. DeepInteraction [55] captures and maintains unique information from each modality. The unique information is fully exploited and integrated during object detection. BEVfusion [14, 56] projects the inputs of two modalities into BEV space to facilitate fusion. SparseFusion [57] firstly extracts candidate features in each modality and then fuses these candidates by a standard self-attention module. CMT [58] projects different modalities into tokens and fuses them by a transformer decoder. UniTR [59] uses a unified transformer encoder to fuse multi-modality inputs simultaneously.

IS-Fusion [15] conducts hierarchical scene fusion and instance-guided fusion to capture contextual information of different scales. GraphBEV [60] utilizes the deformable module to tackle the misalignment caused by inaccurate calibration relationship. DAL [25] imitates the labeling process to conduct feature fusion and object prediction. The core of these methods is to find a unified space for feature fusion, including BEV, voxel, token, etc. Currently, compared to early LiDAR-camera based methods, this type of method shows the ability to solve difficult situations and achieves better performance.

Despite the significant progress of fusing architecture, there is still a gap in eliminating the pixel-point misalignment and the mutual suppression of different sub-tasks. For the first conflict, existing approaches always overlook it or use depth supervision [19]. For the second conflict, existing approaches always adopt decoupled or separate heads [18, 61] that are used in 2D or single-modality detection without hesitation. In contrast, we design two sophisticated modules to tackle these conflicts.

2.4. Misalignment issue

The misalignment of different modalities is an important concern in LiDAR-camera 3D object detection [62, 63], which could be roughly divided into alignment offset and non-uniqueness alignment. The former happens due to the inaccurate camera calibration, making the correspondences between 2D and 3D have some offsets. To solve it, researchers tend to use approaches such as projection offsets and neighboring projections [62]. Specifically, GraphAlign [64] and GraphAlign++ [65] conduct local graph modeling and project it onto the image plane. Autoalign [66] maps cross-modal relation with a learnable alignment map. AutoalignV2 [54] adopts learnable sampling points to model the cross-modality relation. GraphBEV [60] uses neighbor depth features and deformable module to tackle alignment offsets. ContrastAlign [67] enhances the alignment of modalities via contrastive learning. Unlike the above-mentioned methods, in this paper, we focus on non-uniqueness alignment, that is, for opaque objects, the features of one pixel are mapped to multiple points on its corresponding pixel ray. Some uni-modality detections propose a similar conception and call it depth ambiguity. For example, DFA3D [68] extends 2D image features into 3D feature maps and uses 3D deformable attention to aggregate them, which alleviates the depth ambiguity problem from the root. In contrast, we use a more intuitive dual-stream method. In each branch, pixels are mapped to approximately unique points in the 3D space. Thus, our method can reduce the

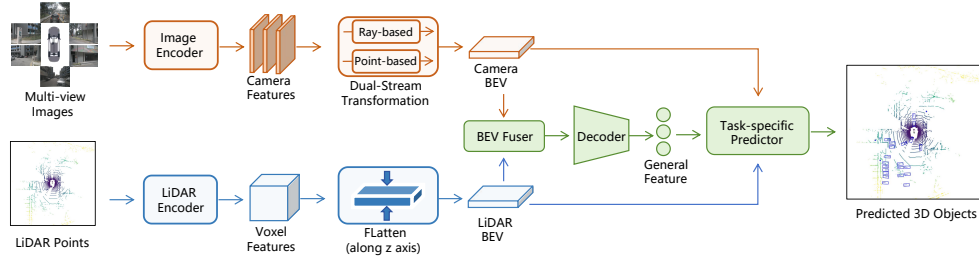


Figure 2: The overall framework of our proposed CoreNet. The key components of our method are: (1) dual-stream transformation which tackles the point-pixel misalignment in 2D-to-BEV transformation, (2) task-specific predictor which tackles the sub-task suppression via explicitly constructing task-specific query.

incorrect correspondences between LiDAR point clouds and images.

3. Method

The overall architecture of our proposed CoreNet is shown in Fig. 2. In this section, we first introduce the overall architecture of our proposed CoreNet in Sec. 3.1. After that, we show the details of the dual-stream transformation module in Sec. 3.2. Finally, we elaborate on the key components of the task-specific predictor in Sec. 3.3.

3.1. Overall Architecture

We first project camera and LiDAR inputs into BEV features to facilitate subsequent steps. The reasons for selecting BEV features are as follows: (1) they are conducive to performing subsequent perception tasks, and (2) they allow for the effective use of mature 2D feature neural networks to deeply process multi-modality features.

For the LiDAR branch, we voxelize the point clouds $P \in R^{N_p \times 5}$ to obtain voxel feature $V \in R^{X \times Y \times Z \times C_v}$, where N_p is the number of the points. Then, we use 3D sparse convolutional blocks [44] as LiDAR encoder to obtain middle feature $M \in R^{X \times Y \times Z \times C_m}$. Finally, we compress the feature M in Z-axis to obtain LiDAR BEV $B_l \in R^{X \times Y \times C_l}$. For the camera branch, the multi-view image inputs $I \in R^{N_i \times H \times W \times 3}$ are encoded into multi-view features $F \in R^{N_i \times H' \times W' \times C_f}$ by the camera encoder, where N_i is the number of images. After that, we obtain the camera BEV $B_c \in R^{X \times Y \times C_c}$ based on the feature F through dual-stream transformation.

Given the camera and LiDAR BEV, we input them into the BEV fuser to obtain the fused BEV. Following previous methods [14, 56], the BEV fuser consists of the CNN-based encoder and SECONDFPN [44] neck. Then, the fused BEV is inputted into the decoder head [20] to obtain general features of objects. Specifically, given the fused BEV B_f , a CNN-based heatmap encoder is first used to extract category-aware heatmap $H \in R^{X \times Y \times N}$ [20, 26], where $X \times Y$ is the size of BEV and N is the number of categories. We select top K local maximum elements as the object candidates, whose values are greater than or equal to their 8 nearest neighbors. Different from GraphBEV [60] and GraphAlign [64], both of which use K nearest neighbors in the feature alignment stage and aim to alleviate the impact of inaccurate camera calibration, our method uses K nearest neighbors in the candidate selecting process to prevent the selected candidates from being too dense or clustered. We denote the indexes of these candidates as $I_p = \{i_k\}_{k=1}^K$. At least, a transformer decoder is used to get the contextual information related to the candidates. The outputs of the transformer decoder are the general features f_g which are universal and could be used in both sub-task heads.

Finally, the camera BEV B_c , LiDAR BEV B_l , and the general feature f_g are inputted into the task-specific predictor to predict the final 3D objects.

3.2. Dual-Stream Transformation

The purpose of the dual-stream transformation is to make a pixel feature from the opaque object projected or approximately scattered into the single point of the same pixel-object ray in the world space. This way will better conform to the occlusion relationship between distant and nearby objects in the real world, thereby reducing the impact of redundant information on feature fusion. As shown in Fig. 3, dual-stream transformation consists of ray-based and point-based 2D-to-BEV transformations. Given the multi-view camera features F , we upsample them to the same shape as the image inputs via deconvolution block to obtain a high-resolution (HR) feature. Meanwhile, the channel of the feature map is reduced to decrease resource consumption. The HR feature is inputted to a point-based stream to make it create more precise connections between the point and the pixel, while the origin low-resolution (LR) feature F is inputted to ray stream as too large feature sizes can consume a lot of computation time. Each stream will output its corresponding BEV. The CNN-based BEV encoder will fuse the ray and point BEV and output the final camera BEV.

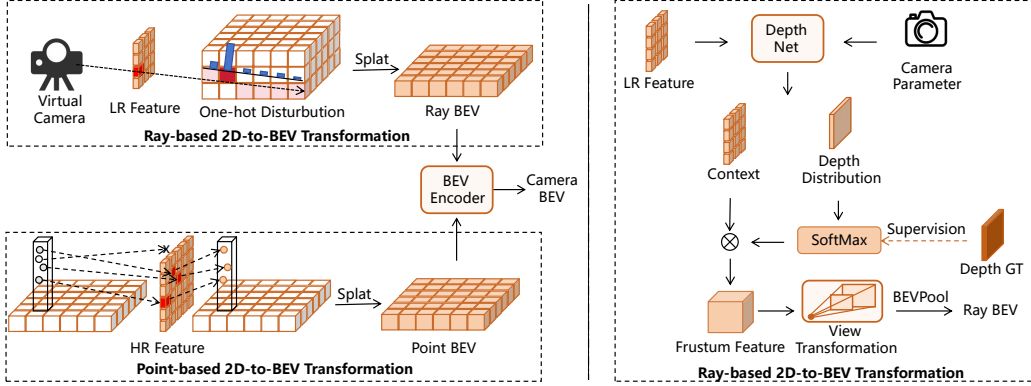


Figure 3: The overall framework of our proposed dual-stream transformation.

3.2.1. Ray-Based 2D-to-BEV Transformation

Given the LR feature, following BEVDepth [19], we adopt depth net to encode the LR feature and camera parameter. The output of depth net is the context feature $F_t \in R^{N_i \times H' \times W' \times C_t}$ and the depth distribution $D_p \in R^{N_i \times H' \times W' \times D}$, where D is the number of points along the depth axis. We suppose that the depth distribution of each pixel should be close to the one-hot distribution because of opacity and occlusion. In view of this, we generate the one-hot depth ground-truth D_g based on the LiDAR point clouds and camera parameters. The depth loss can be calculated via Eq. 1.

$$L_{depth} = \Phi(D_g, D_p), \quad (1)$$

where Φ is the binary cross entropy loss. Based on F_t and D_p , we obtain frustum feature $T \in R^{N_i \times H \times W \times D \times C_t}$. At last, T is projected into world space, and the information in the Z-axis is compressed using BEVPool [14] to get the final ray BEV.

3.2.2. Point-Based 2D-to-BEV Transformation

In the point-based stream, we use the LiDAR points which are located on the surface of the objects as the guidance. We suppose it can help the pixel features be projected to the correct position in the scene. We first partition the scene into the BEV grids, each BEV grid represents a certain region in the real world. Based on the LiDAR point clouds P and pre-defined BEV grids, we first divide P into several bins $\{b_1, b_2, \dots, b_{n^2}\}$, where n is the number of grids on the BEV edge. Each bin contains an indefinite number

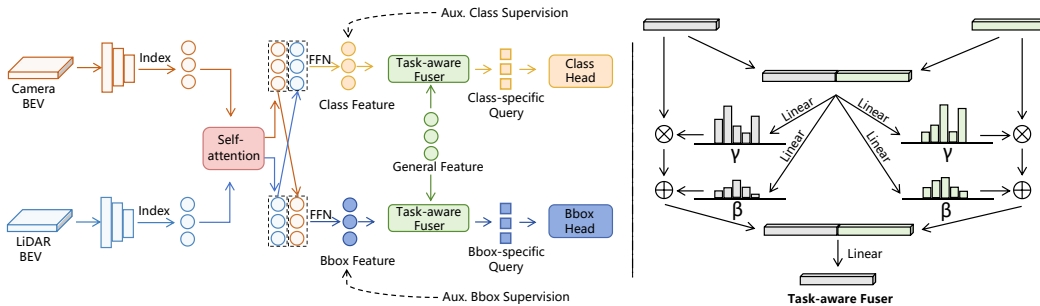


Figure 4: The overall framework of our proposed task-specific predictor.

of points $\{p^1, p^2, \dots, p^l\}$ and corresponds to a certain BEV grid. For each bin, we project these points to the image space, retaining only the points that fall onto the image plane, and use the corresponding pixel features in the HR feature as the features of the valid points. Then, we aggregate the features of these valid points and let the aggregated feature be the feature of the corresponding BEV grid. We repeat the above operation for each bin and obtain the point BEV. However, the LiDAR points are sparse and not every point can be projected to the image plane, so the valid grids in point BEV are sparse. To tackle this problem, we fuse the point BEV with dense ray BEV to get the final camera BEV. In addition, from the pixel coordinate to the 3D coordinate, point-based transformation can be equivalently converted into calculating the depth of the pixels owning correspondences with points and then projecting these pixels and their corresponding features into 3D space. Therefore, this process also uses depth information. Compared with the ray-based transformation, point-based transformation only handles pixels owning the correspondences with points, while the ray-based transformation deals with each pixel based on depth prediction. The point-based transformation provides an accurate and fast view transformation, while the ray-based transformation helps to supplement the space that is not scanned by LiDAR with 2D features.

3.3. Task-Specific Predictor

The overall framework of our proposed task-specific predictor is shown in Fig. 4. The purpose of the task-specific predictor is to tackle the mutual suppression between classification prediction and bounding box regression during joint training. To this end, we explicitly and controllably construct task-specific features and integrate them with general features to build

task-specific queries. Sub-task heads will use the corresponding task-specific queries to predict the certain attributes of the objects.

3.3.1. Task-Specific Feature

Given camera BEV B_c and LiDAR BEV B_l , we first use CNN-based encoders to obtain specific features, and the parameters of these two specific encoders are not shared. The outputs of these encoders are denoted as \widetilde{B}_c and \widetilde{B}_l . To maintain the consistency of the candidate position and facilitate the subsequent fusion between general and task-specific features, we directly use the candidate indexes I_p generated in Sec. 3.1 to select candidates in specific feature extractor. Given the \widetilde{B}_c , \widetilde{B}_l , and the indexes of candidates I_p , we first generate camera candidates $Q_c = \{Q_{c,k}\}_{k=1}^K$ from \widetilde{B}_c and I_p . We then generate LiDAR candidates $Q_l = \{Q_{l,k}\}_{k=1}^K$ from \widetilde{B}_l and I_p . After that, we concatenate Q_c and Q_l together and use a standard self-attention module to fuse these two modal candidates. Then, the corresponding LiDAR and camera candidates are fused by the feed-forward network (FFN) to obtain the class feature f_c and Bbox feature f_b .

3.3.2. Task-Specific Supervision

Although the method in Sec. 3.3.1 explicitly constructs the task-specific features, it cannot guarantee the correlation between these features and their corresponding sub-tasks. In other words, we hope that the sub-task preferences of these features are controllable. The best way of achieving this goal is to use supervision which makes class features focus on classification prediction and Bbox features focus on bounding box prediction. In view of this, we propose task-specific supervision which is only conducted in the training stage.

We use a feed-forward network (FFN) to construct a class auxiliary task head and a Bbox auxiliary task head. Given class feature f_c and Bbox feature f_b , f_c is used to predict class, and f_b is used to predict Bbox. The class predicted result and its corresponding Bbox predicted result will be combined as an auxiliary predicted result o for one object. We use bipartite matching [34] between the predictions and ground-truth objects \hat{o} through the Hungarian algorithm. We calculate the auxiliary loss based on Eq. 2.

$$L_{aux}(o, \hat{o}) = \lambda_1 L_{cls}(c, \hat{c}) + \lambda_2 L_{Bbox}(b, \hat{b}), \quad (2)$$

where λ_1 and λ_2 are the hyper-parameters to balance class-aux loss function L_{cls} and Bbox-aux loss function L_{Bbox} , c , b are the predicted object's category

and 3D bounding box, and \hat{c} , \hat{b} denote the corresponding ground-truth. We use focal loss [41] as L_{cls} and L1 Loss as L_{Bbox} .

3.3.3. Task-Specific Fuser

Given the general feature and the task-specific feature, we use a task-specific fuser to adaptively fuse the specific and general features, which can select different information of interest for different sub-tasks. We first concatenate general and specific features. Then, we predict the attention vector γ and β via Eq. 3.

$$\gamma = \psi_1([f_g, f_s]), \beta = \psi_1([f_g, f_s]), \quad (3)$$

where $\psi_{i=1,2}(\cdot)$ are the linear mapping functions, $[\cdot, \cdot]$ is the concatenate function and f_s is the task-specific feature. We predict a total of two groups γ and β , one of which is used to adjust the information preference for specific features, and the other is used to adjust the information preference for general features. After that, we obtain the task-specific query Q_s via Eq. 4.

$$Q_s = \psi([\gamma_s \times f_s + \beta_s, \gamma_g \times f_g + \beta_g]), \quad (4)$$

where $\psi(\cdot)$ is the linear function, $[\cdot, \cdot]$ is the concatenate function, $[\gamma_s, \beta_s]$ and $[\gamma_g, \beta_g]$ are the attention vectors corresponding to task-specific and general feature, respectively. Finally, the task-specific query will be inputted to the sub-task head for predicted 3D objects.

4. Experiments

4.1. Dataset and metrics

We conduct extensive experiments on a large-scale autonomous driving dataset nuScenes [24], which is widely used for 3D LiDAR-camera object detection and 3D multi-object tracking task. There are a total of 10 classes of objects and around 1.4 million annotated 3D bounding boxes in nuScenes. NuScenes totally has 1000 scenes in different conditions, such as sunny, rainy, day, and night. For each frame, nuScenes has 6 images and 1 point cloud from 32 beams LiDAR. The multi-view camera group has the same field-of-view as LiDAR point clouds, 360°. We follow the official instruction to divide 1000 scenes into 700/150/150 for training/validation/testing. Following common practice, we transform the points from the previous 9 frames to the current frame for training and evaluation. For 3D object detection,

we follow BEVFusion [14] to use nuScenes detection score (NDS) and mean average precision (mAP) as the metrics. Unlike 2D detection, the mAP is defined by the distance of the center instead of the Intersection over Union (IOU). The final mAP is the average result of distances 0.5m, 1m, 2m, and 4m among ten classes. For NDS, it is the weighted sum of mAP and other official predefined metrics including average translation error (ATE), average scale error (ASE), average orientation error (AOE), average velocity error (AVE), average attribute error (AAE). For the 3D multi-object tracking task, we follow Centerpoint [26] to use average multi-object tracking accuracy (AMOTA), average multi-object tracking precision (AMOTP), and ID switch as the metrics.

4.2. Implement Details

We implement our network based on MMDetection3D [77] and BEVFusion [14] codebase. For multi-object tracking tasks, we adopt the tracking test script in the Centerpoint[26] codebase to provide a fair comparison. We adopt Swin-T [78] as our image encoder and VoxelNet [43] as our LiDAR encoder that is mentioned in Sec. 3.1. We first pre-train the image encoder and LiDAR encoder, following [14, 25]. Then, we train CoreNet for another 6 epochs based on these two pre-trained encoders. Following previous methods [14, 56], we also use CBGS [79] in the pre-train and fusion processes. The voxel size is set to (0.075m, 0.075m, 0.2m), and the BEV feature map is set to 180×180 . During the CoreNet training, we use the same training strategy and data augmentation as BEVFusion [14]. Specifically, the learning rate is adjusted by cycle policy with the initial value 2.0×10^{-4} . We conduct optimization based on AdamW with weight decay value 10^{-2} . During the training process, we don't freeze any pre-trained backbone, and the entire model is trained in an end-to-end manner. All the codes are implemented by PyTorch, and the model is trained with a batch size of 16 on 8 NVIDIA A100 GPUs. For the evaluation results, we only show the performance of the single model without any test-time augmentation or model ensemble.

4.3. Performance Comparison

4.3.1. Detection results comparison

We compare CoreNet with other existing approaches on nuScenes [24] test set as shown in Table 1. CoreNet performs better than all the other single-modality and multi-modality methods by achieving 73.3% mAP and 75.6%

Table 1: Detection performance comparison on nuScenes test set. ‘C.V.’, ‘T.L.’, ‘B.R.’, ‘M.T.’, ‘Ped.’, and ‘T.C.’ indicate the construction vehicle, trailer, barrier, motorcycle, pedestrian, and a traffic cone, respectively. The best performance is highlighted in bold, while the second best is marked underlined. Results are the performance of the single model without any test-time augmentation or model ensemble.

Method	Car	Truck	C.V.	Bus	T.L.	B.R.	M.T.	Bike	Ped.	T.C.	mAP	NDS
LiDAR Methods												
CenterPoint[26]	84.6	51.0	17.5	60.2	53.2	70.9	53.7	28.7	83.4	76.7	58.0	65.5
VoxelNetXt[69]	84.6	53.0	28.7	64.7	55.8	74.6	73.2	45.7	85.8	79.0	64.5	70.0
TransFusion-L[20]	86.2	56.7	28.2	66.3	58.8	78.2	68.3	44.2	86.1	82.0	65.5	70.2
HEDNet[70]	87.1	56.5	33.6	70.4	63.5	78.1	70.4	44.8	87.9	85.1	67.7	72.0
FocalFormer3D[71]	87.2	57.1	34.4	69.6	64.9	77.8	76.2	49.6	88.2	82.3	68.7	72.6
DSVT [72]	-	-	-	-	-	-	-	-	-	-	68.4	72.7
LION[73]	87.1	61.1	36.3	68.9	65.0	79.5	74.0	49.2	90.0	87.3	69.8	73.9
LiDAR-Camera Methods												
GraphAlign[64]	87.6	57.7	26.1	66.2	57.8	74.1	72.5	49.0	87.2	86.3	66.5	70.6
AutoAlign[66]	85.9	55.3	29.6	67.7	55.6	-	71.5	51.5	86.4	-	65.8	70.9
UVTR[74]	87.5	56.0	33.8	67.5	59.5	73.0	73.4	54.8	86.3	79.6	67.1	71.1
TansFusion[20]	87.1	60.0	33.1	68.3	60.8	78.1	73.6	52.9	88.4	86.7	68.9	71.7
BEVFusion(PKU)[56]	88.1	60.9	34.4	69.3	62.1	78.2	72.2	52.2	89.2	85.5	69.2	71.8
GraphAlign++[65]	87.5	58.5	32.3	68.9	58.3	74.3	76.4	53.9	88.3	86.3	68.5	72.2
Autoalignv2[54]	87.0	59.0	33.1	69.3	59.3	-	72.9	52.1	87.6	-	68.4	72.4
BEVFusion(MIT)[14]	88.6	60.1	39.3	69.8	63.8	80.0	74.1	51.0	89.2	86.5	70.2	72.9
ObjectFusion[75]	89.4	59.0	40.5	71.8	63.1	80.0	78.1	53.2	90.7	87.7	71.0	73.3
DeepInteraction[55]	87.9	60.2	37.5	70.8	63.8	80.4	75.4	54.5	91.7	87.2	70.8	73.4
GraphBEV[60]	89.2	60.0	40.8	72.1	64.5	80.1	76.8	53.3	90.9	88.9	71.7	73.6
ContrastAlign[67]	89.0	60.9	41.1	70.1	64.6	82.2	75.9	53.8	90.9	89.3	71.8	73.8
SparseFusion[57]	88.0	60.2	38.7	72.0	64.9	79.2	78.5	59.8	90.9	87.9	72.0	73.8
FocalFormer3D-F[71]	88.5	61.4	35.9	71.7	66.4	79.3	80.3	57.1	89.7	85.3	71.6	73.9
MSMDFusion[76]	88.4	61.0	35.2	71.4	64.2	80.7	76.9	58.3	90.6	88.1	71.5	74.0
CMT[58]	88.0	63.3	37.3	75.4	65.4	78.2	79.1	60.6	87.9	84.7	72.0	74.1
UniTR[59]	87.9	60.2	39.3	72.2	65.1	76.8	75.8	52.3	89.4	89.7	70.9	74.5
DAL[25]	-	-	-	-	-	-	-	-	-	-	72.0	74.8
IS-Fusion[15]	88.3	62.7	38.4	74.9	67.3	78.1	82.4	59.5	89.3	89.2	<u>73.0</u>	<u>75.2</u>
CoreNet(ours)	89.7	63.4	39.9	73.9	66.7	79.1	80.3	59.3	91.7	88.5	73.3	75.6

NDS. Compared to BEVFusion(MIT) [14] which is the baseline, CoreNet improves the results by 2.7% NDS and 3.1% mAP. Compared to recent SOTA methods, IS-Fusion [15] and DAL [25], CoreNet also achieves better results.



Figure 5: The visualization of our proposed method on nuScenes validation set.

It should be noted that CoreNet is a flexible model. The dual-stream transformation and task-specific predictor proposed by CoreNet can be extracted and combined with other methods.

As shown in Table 2, we compare the detection performance on the nuScenes validation set and achieve the best performance by achieving 74.5% NDS and 72.6% mAP. We find that CoreNet surpasses the SOTA methods on different sizes of image inputs. Compared with different backbones including ResNet-50 [80] and VoVNet [81], CoreNet can also achieve satisfactory results. As shown in Table 3, we compare the inference speed and parameter size between CoreNet and the existing SOTA IS-Fusion. It could be observed that CoreNet has a faster inference speed. We visualize some qualitative results of CoreNet to prove its superiority, as shown in Fig. 5. We also compare the visualization among ground-truth, SparseFusion, IS-Fusion, and CoreNet in Fig. 6. Our proposed model shows strong competitiveness in 3D object detection tasks, which fully demonstrates the following viewpoint: reducing the depth ambiguity in 2D-to-BEV transformation and alleviating suppression between different sub-tasks can boost performance.

Table 2: Detection performance comparison on nuScenes validation set. The best performance is highlighted in bold, while the second best is marked underlined.

Method	Image encoder	Voxel encoder	Image size	mAP(%) \uparrow	NDS(%) \uparrow
CMT [58]	ResNet-50 [80]	VoxelNet [43]	320 \times 800	67.9	70.8
Transfusion [20]	ResNet-50 [80]	VoxelNet [43]	448 \times 800	68.5	71.4
BEVFusion [14]	Swin-T [80]	VoxelNet [43]	256 \times 704	68.5	71.4
DeepInteraction [55]	ResNet-50 [80]	VoxelNet [43]	448 \times 800	69.9	72.6
GraphBEV [60]	Swin-T [80]	VoxelNet [43]	256 \times 704	70.1	72.9
SparseFusion [57]	Swin-T [78]	VoxelNet [43]	448 \times 800	71.0	73.1
UniTR [59]	DSVT [72]	DSVT [72]	256 \times 704	70.5	73.3
DAL [25]	ResNet-50 [80]	VoxelNet [43]	256 \times 704	70.0	73.4
IS-Fusion [15]	Swin-T [78]	VoxelNet [43]	256 \times 704	72.4	73.7
CoreNet (ours)	Swin-T [78]	VoxelNet [43]	256 \times 704	71.5	73.9
CMT [58]	VoVNet [81]	VoxelNet [43]	640 \times 1600	70.3	72.9
CoreNet (ours)	VoVNet [81]	VoxelNet [43]	640 \times 1600	72.3	74.2
DAL [25]	ResNet-50 [80]	VoxelNet [43]	384 \times 1056	71.5	74.0
CoreNet (ours)	ResNet-50 [80]	VoxelNet [43]	384 \times 1056	71.7	73.9
IS-Fusion [15]	Swin-T [78]	VoxelNet [43]	384 \times 1056	72.8	<u>74.0</u>
CoreNet (ours)	Swin-T [78]	VoxelNet [43]	384 \times 1056	<u>72.6</u>	74.5

Table 3: Comparison of inference speed and parameter size on nuScenes validation set with Swin-T backbones. We test all the models and report results on a single NVIDIA Tesla A100 GPU without considering the time cost of voxelization in the voxel backbone. The size of input images is set to 384 \times 1056.

Method	Latency(ms)				FPS \uparrow	#parm.	NDS(%)
	Backbone	ViewTrans	Encoder	Decoder			
IS-Fusion[15]	87	35	193	8	3.1	53.4M	74.0
CoreNet	74	110	22	15	4.5	87.5M	74.5

4.3.2. 3D multi-object tracking comparison

We also conduct 3D multi-object tracking (MOT) experiments on the nuScenes tracking benchmark. Following previous works [20, 75], we use the same tracking-by-detection algorithm, which directly connects objects in consecutive frames based on the greedy algorithm. As shown in Table 4, our proposed CoreNet achieves competitive results (76.3% in AMOTA, 46.3% in AMOTP, 656 in ID switch). Compared to our baseline BEVFusion [14], CoreNet improves AMOTA by 3.5%. Compared to IS-Fusion [15] which shows good performance in 3D detection task, CoreNet improves AMOTA

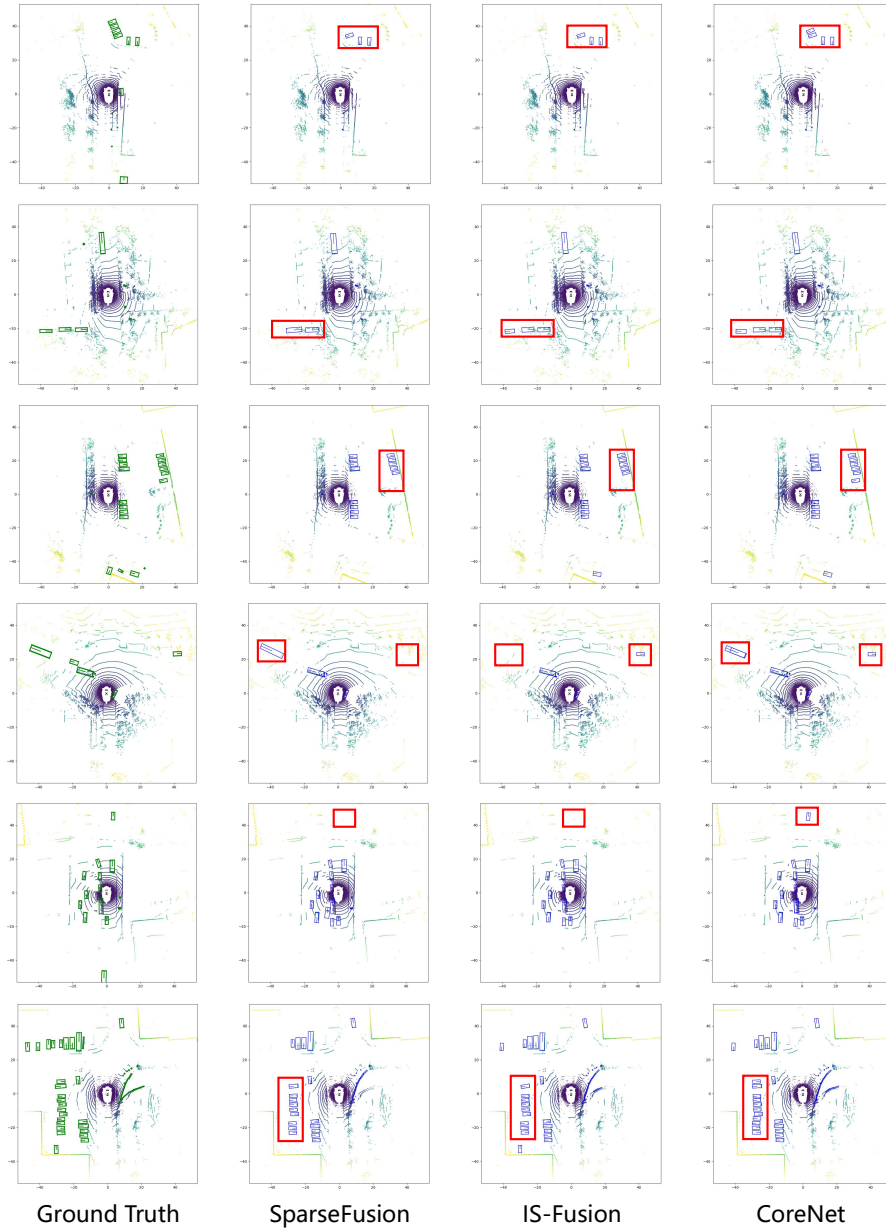


Figure 6: The visualization of our proposed method on nuScenes validation set. The red box indicates the areas where we successfully predicted but previous methods failed.

by 2.7%. This indicates that the detection results of CoreNet have better stability and continuity, and CoreNet could be a strong solution for the 3D

Table 4: Tracking performance comparison on nuScenes validation set. The Modality column: “L” means only use LiDAR data; “LC” means use both LiDAR and camera data. The best performance is highlighted in bold, while the second best is marked underlined.

Method	Modality	AMOTA (%) \uparrow	AMOTP (%) \downarrow	ID switch \downarrow
Centerpoint [26]	L	63.7	60.6	640
TransFusion-L [20]	L	69.9	59.9	821
TransFusion [20]	LC	71.8	60.3	794
BEVFusion [14]	LC	72.8	59.4	764
ObjectFusion [75]	LC	<u>74.2</u>	54.3	611
SparseFusion [57]	LC	61.1	56.0	930
IS-Fusion [15]	LC	73.6	<u>52.7</u>	1017
CoreNet (ours)	LC	76.3	46.3	<u>656</u>

Table 5: Ablation study for each module in CoreNet. DST indicates dual-stream transformation, and TSP indicates task-specific predictor.

DST	TSP	mATE	mASE	mAOE	mAVE	mAAE	mAP	NDS
		0.278	0.256	0.319	0.201	0.182	68.7	72.0
✓		0.274	0.254	0.284	0.187	0.184	69.4	72.9
	✓	0.274	0.253	0.268	0.184	0.182	69.8	73.3
✓	✓	0.273	0.254	0.287	0.187	0.183	71.5	73.9

MOT task.

4.4. Ablation Study

In this section, we investigate the effectiveness of each proposed component. Our ablation study is conducted on nuScenes validation set by using Swin-T [78] backbone and setting image size to 256×604 . For the baseline of our method, we have two changes compared to the original BEVFusion [14]: (1) we use velocity augment [25] to increase the precision of velocity prediction and (2) we change the original shallow BEV Fuser into a sophisticated CNN-based network. As shown in Table 5, we first evaluate the performance of the two main modules, i.e., dual-stream transformation (DST) and task-specific predictor (TSP). DST improves the results by 0.7% mAP and 0.9% NDS, while TSP improves the results by 1.1% mAP and 1.3% NDS. Adopting DST and TSP simultaneously can improve the results by 2.8% mAP and 1.9% NDS, demonstrating the effect of tackling depth ambiguity and sub-task suppression.

Table 6: Component-wise ablation study on dual-stream transformation.

Ray	Point	mATE	mASE	mAOE	mAVE	mAAE	mAP	NDS
✓		0.275	0.254	0.307	0.197	0.184	68.9	72.3
	✓	0.270	0.254	0.300	0.200	0.185	69.1	72.5
✓	✓	0.274	0.254	0.284	0.187	0.184	69.4	72.9

Table 7: Component-wise ablation study on task-specific predictor. TS is the abbreviation of task-specific.

component	mATE	mASE	mAOE	mAVE	mAAE	mAP	NDS
+ TS feature	0.278	0.256	0.297	0.192	0.183	69.2	72.5
+ TS supervision	0.277	0.253	0.291	0.189	0.181	69.6	72.9
+ TS fuser	0.274	0.253	0.268	0.184	0.182	69.8	73.3

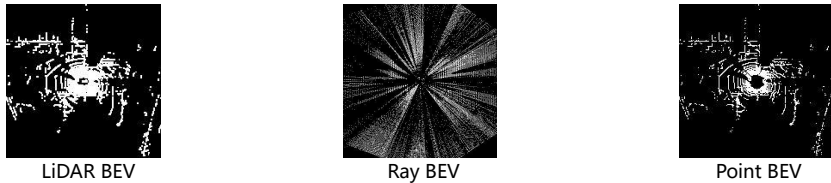


Figure 7: Visualization of the ray BEV and the point BEV. Bright grids indicate the presence of features here.

The dual-stream transformation consists of two main streams, i.e., ray-based and point-based streams. The purpose of these two streams is both to alleviate the depth ambiguity caused by point-pixel misalignment. As shown in Table 6, we investigate the effectiveness of these two streams. Ray-based transformation improves the results by mAP 0.2% and 0.3% NDS, while point-based stream improves the results by 0.4% mAP and 0.5% NDS. This result highlights the crucial role of projecting 2D pixel features into 3D points should comply with occlusion relationships. As shown in Fig. 7, we visualize the ray BEV and the point BEV. It can be observed that the number of valid grids of ray BEV is higher, while the valid grid distribution of point BEV is closer to that of LiDAR. It should be noted that ray BEV also generates multiple features on each pixel-object ray, but through one-hot supervision, pixel features are mainly concentrated on a certain point. The motivation of task-specific predictor is to relieve the mutual suppression between class and Bbox prediction by constructing a task-specific query. It consists of three key parts: (1) task-specific feature, (2) task-specific supervision, and (3) task-

Table 8: Robustness analysis on nuScenes validation set with different lighting and weather conditions. We use mAP(%) as the metric for evaluation.

Method	Modality	Sunny	Rainy	Day	Night
CenterPoint [26]	L	62.9	59.2	62.8	35.4
BEVDet [21]	C	32.9	33.7	33.7	13.5
BEVFusion [14]	LC	68.2	69.9	68.5	42.8
GraphBEV [60]	LC	70.1	70.2	69.7	45.1
SparseFusion [57]	LC	70.3	70.4	70.5	<u>44.7</u>
IS-Fusion [15]	LC	72.2	<u>71.7</u>	<u>72.5</u>	44.4
CoreNet (Ours)	LC	72.2	73.6	72.6	45.0

specific fuser. As shown in Table 7, we use a step-wise way to evaluate their performance. All these three components contribute to the final results. The full task-specific predictor improves the results by 1.1% mAP and 1.3% NDS. This phenomenon highlights the importance of reducing mutual suppression across different sub-tasks. Additionally, these two components can easily be inserted into other BEV-based methods for further application.

4.5. Robustness Analysis

In this section, we conduct a robustness analysis to simulate the outside environment in real-world usage scenarios. The robustness is measured under different conditions, including lighting, weather conditions, object distances, and sizes. All these experiments are conducted on the nuScenes validation set.

We first evaluate the performance under lighting and weather changes, which are challenging as they can affect the quality of data received by sensors. Following BEVFusion [14], we split the scenes into Sunny, Rainy, Day, and Night by searching the keywords 'rain' and 'night' in the scene description. As shown in Table 8, our proposed CoreNet surpasses the previous methods under different conditions. Compared to the baseline BEVFusion, CoreNet improves mAP by 4.0%, 3.7%, 4.1%, and 2.2% on the Sunny, Rainy, Day, and Night conditions, respectively. Compared to the SOTA method IS-Fusion, CoreNet improves mAP by 1.9 % in the rainy condition. This indicates that our method has better stability in scenarios with noise.

We then analyze the performance under different distances and sizes. Following BEVFusion [14], we classify objects into three categories based on their distance to the vehicle: Near (0-20m), Middle (20-30m), and Far (>30m). We also divide the objects into Small (0-4m) and Large (>4m)

Table 9: Robustness analysis on nuScenes validation set with different ego distances and object sizes. We use mAP(%) as the metric for evaluation.

Method	Modality	Near	Middle	Far	Small	Large
TransFusion-L [20]	L	77.1	60.4	43.2	56.1	53.1
BEVFusion [14]	LC	78.5	64.6	50.5	61.9	57.9
GraphBEV [60]	LC	78.6	65.3	42.1	-	-
SparseFusion [57]	LC	81.3	66.8	51.6	64.8	58.2
IS-Fusion [15]	LC	<u>81.5</u>	69.8	<u>55.6</u>	65.9	<u>62.0</u>
CoreNet (Ours)	LC	82.2	<u>68.3</u>	56.3	<u>65.7</u>	62.2

groups according to their sizes. As shown in Table 9, compared to the baseline and latest SOTA methods [15, 57] CoreNet achieves the best performance. In the hard case, i.e., detecting objects at a long distance, CoreNet surpasses BEVFusion and IS-Fusion by 5.8% and 0.7% mAP, respectively. Long distances will reduce the useful information captured by sensors. Better results in this scene indicate that when there is insufficient effective information about objects, the prediction results of CoreNet are more robust.

We then analyze the performance under different corruptions, as shown in Table 10. We conduct our experiments in a widely used benchmark with common corruptions in autonomous driving, i.e., nuScenes-C [82]. There totally has 27 types of common corruptions for both LiDAR and camera inputs in real-world scenarios, which could be divided into five classifications, including, weather, sensor, motion, object, and alignment. It could be observed that our proposed CoreNet achieves the best performance by achieving 64.98% mAP_{cor}. Particularly, in some extremely hard cases, our method shows great robustness. For example, CoreNet improves the mAP_{cor} by 11.55 % compared to BEVFusion [14] under motion compensation.

5. Conclusion

In this paper, we proposed a novel model termed **Conflict Resolution Network** (CoreNet) for LiDAR-camera 3D object detection. We first conduct in-depth thinking on the task and summarize two conflicts, i.e., point-pixel misalignment and sub-task suppression that are overlooked by previous methods. Point-pixel misalignment ignores the occlusion and opacity relationship of objects and projects single-pixel features incorrectly, resulting in depth ambiguity and information interference. Sub-task suppression can lead to mutual disturbance between classification prediction and bounding box

Table 10: Comparison of robust results under different corruptions on nuScenes-C [82] benchmark. The original performance, the performance under each corruption and the overall averaged corruption robustness mAP_{cor} are shown.

Corruption		LiDAR-only			Camera-only			LC Fusion			
		PointPillars	SSN	CenterPoint	PGD	DETR3D	Bevformer	FUTR3D	TransFusion	BEVFusion	Ours
None (mAP_{clean})		27.69	46.65	59.28	23.19	34.71	41.65	64.17	66.38	68.45	72.55
Weather	Snow	27.57	46.38	55.90	2.30	5.08	5.73	52.73	63.30	62.84	64.03
	Rain	27.71	46.50	56.08	13.51	20.39	24.97	58.40	65.35	66.13	69.09
	Fog	24.49	41.64	43.78	12.83	27.89	32.76	53.19	53.67	54.10	61.80
	Sunlight	23.71	40.28	54.20	22.77	34.66	41.68	57.70	55.14	64.42	70.88
Sensor	Density	27.27	46.14	58.60	-	-	-	63.72	65.77	67.79	72.21
	Cutout	24.14	40.95	56.28	-	-	-	62.25	63.66	66.18	70.92
	Crosstalk	25.92	44.08	56.64	-	-	-	62.66	64.67	67.32	71.18
	FOV Lost	8.87	15.40	20.84	-	-	-	26.32	24.63	27.17	29.15
	Gaussian (L)	19.41	39.16	45.79	-	-	-	58.94	55.10	60.64	68.84
	Uniform (L)	25.60	45.00	56.12	-	-	-	63.21	64.72	66.81	71.82
	Impulse (L)	26.44	45.58	57.67	-	-	-	63.43	65.51	67.54	72.03
	Gaussian (C)	-	-	-	4.33	14.86	15.04	54.96	64.52	64.44	65.94
	Uniform (C)	-	-	-	8.48	21.49	23.00	57.61	65.26	65.81	68.30
	Impulse (C)	-	-	-	3.78	14.32	13.99	55.16	64.37	64.30	65.35
Motion	Compensation	3.85	10.39	11.02	-	-	-	31.87	9.01	27.57	39.12
	Moving Obj.	19.38	35.11	44.30	10.47	16.63	20.22	45.43	51.01	51.63	50.08
	Motion Blur	-	-	-	9.64	11.06	19.79	55.99	64.39	64.74	67.03
Object	Local Density	26.70	45.42	57.55	-	-	-	63.60	65.65	67.42	71.63
	Local Cutout	17.97	32.16	48.36	-	-	-	61.85	63.33	63.41	67.79
	Local Gaussian	25.93	43.71	51.13	-	-	-	62.94	63.76	64.34	70.58
	Local Uniform	27.69	46.87	57.87	-	-	-	64.09	66.20	67.58	72.29
	Local Impulse	27.67	46.88	58.49	-	-	-	64.02	66.29	67.91	72.31
	Shear	26.34	43.28	49.57	16.66	17.46	24.71	55.42	62.32	60.72	58.78
	Scale	27.29	45.98	51.13	6.57	12.02	17.64	56.79	64.13	64.57	66.07
	Rotation	27.80	46.93	54.68	16.84	27.28	33.97	59.64	63.36	65.13	69.49
Alignment	Spatial	-	-	-	-	-	-	63.77	66.22	68.39	71.18
	Temporal	-	-	-	-	-	-	51.43	43.65	49.02	56.64
Average (mAP_{cor})		23.42	40.37	49.81	10.68	18.60	22.79	56.99	58.73	61.03	64.98

regression, resulting in sub-optimal results. To solve these issues, we introduce two novel modules: dual-stream transformation and task-specific predictor. Specifically, dual-stream transformation uses a two-branch structure to approximately scatter a pixel feature into a single point of the same ray, while task-specific predictor explicitly and controllably creates task-specific features and combines them with general features to develop task-specific queries. Extensive experiments are carried out on the nuScenes dataset to prove the superiority of our method, the effectiveness of each module, and the robustness of the method. We believe that CoreNet can provide useful inspiration for future methods.

Limitations and further work. Although our method achieves good performance, there is still room for improvement in some extremely difficult conditions such as detecting objects at night or at a far distance. In future work, we will introduce relevant modules and data augmentation methods to address these issues.

Data availability

The code and data used in this study are available at <https://github.com/liyih/CoreNet>.

Declaration of competing interest

I have nothing to declare.

Acknowledgment

This work was supported in part by the Chinese National Natural Science Foundation Project 62206276, 62276254, U23B2054, and the InnoHK program.

References

- [1] Z. Huang, S. Sun, J. Zhao, L. Mao, Multi-modal policy fusion for end-to-end autonomous driving, *Information Fusion* 98 (2023) 101834. <https://doi.org/10.1016/j.inffus.2023.101834>
- [2] D. Fernandes, A. Silva, R. Névoa, C. Simões, D. Gonzalez, M. Guevara, P. Novais, J. Monteiro, P. Melo-Pinto, Point-cloud based 3d object detection and classification methods for self-driving applications: A survey and taxonomy, *Information Fusion* 68 (2021) 161–191. <https://doi.org/10.1016/j.inffus.2020.11.002>
- [3] X. Zhang, L. Wang, J. Chen, C. Fang, L. Yang, Z. Song, G. Yang, Y. Wang, X. Zhang, J. Li, Dual radar: A multi-modal dataset with dual 4d radar for autonomous driving, *arXiv preprint arXiv:2310.07602* (2023). <https://doi.org/10.48550/arXiv.2310.07602>
- [4] X. Wang, Z. Sun, A. Chehri, G. Jeon, Y. Song, Deep learning and multi-modal fusion for real-time multi-object tracking: Algorithms, challenges, datasets, and comparative study, *Information Fusion* 105 (2024) 102247. <https://doi.org/10.1016/j.inffus.2024.102247>

- [5] J. Mao, S. Shi, X. Wang, H. Li, 3d object detection for autonomous driving: A comprehensive survey, *International Journal of Computer Vision* (2023) 1–55.
<https://doi.org/10.1007/s11263-023-01790-1>
- [6] Y. Wu, Fusion-based modeling of an intelligent algorithm for enhanced object detection using a deep learning approach on radar and camera data, *Information Fusion* (2024) 102647.
<https://doi.org/10.1016/j.inffus.2024.102647>
- [7] M. Hao, Z. Zhang, L. Li, K. Dong, L. Cheng, P. Tiwari, X. Ning, Coarse to fine-based image–point cloud fusion network for 3d object detection, *Information Fusion* 112 (2024) 102551.
<https://doi.org/10.1016/j.inffus.2024.102551>
- [8] X. Jiang, D. Wang, K. Bi, S. Wang, M. Zhang, Mshp3d: Multi-stage cross-modal fusion based on hybrid perception for indoor 3d object detection, *Information Fusion* 112 (2024) 102591.
<https://doi.org/10.1016/j.inffus.2024.102591>
- [9] L. Yang, X. Zhang, J. Li, C. Wang, Z. Song, T. Zhao, Z. Song, L. Wang, M. Zhou, Y. Shen, et al., V2x-radar: A multi-modal dataset with 4d radar for cooperative perception, *arXiv preprint arXiv:2411.10962* (2024).
<https://doi.org/10.48550/arXiv.2411.10962>
- [10] Z. Song, G. Zhang, L. Liu, L. Yang, S. Xu, C. Jia, F. Jia, L. Wang, Robofusion: Towards robust multi-modal 3d object detection via sam, *arXiv preprint arXiv:2401.03907* (2024).
<https://doi.org/10.48550/arXiv.2401.03907>
- [11] S. Xu, F. Li, Z. Song, J. Fang, S. Wang, Z.-X. Yang, Multi-sem fusion: multimodal semantic fusion for 3d object detection, *IEEE Transactions on Geoscience and Remote Sensing* (2024).
<https://doi.org/10.1109/TGRS.2024.3387732>
- [12] S. Jiang, S. Xu, L. Liu, Z. Song, Y. Bo, Z.-X. Yang, et al., Sparsein-teraction: Sparse semantic guidance for radar and camera 3d object detection, in: *ACM Multimedia 2024*, 2024.
<https://doi.org/10.1145/3664647.3681565>

- [13] Y. Li, Y. Yang, Z. Lei, Rctrans: Radar-camera transformer via radar densifier and sequential decoder for 3d object detection, in: Proceedings of the AAAI Conference on Artificial Intelligence, 2025.
- [14] Z. Liu, H. Tang, A. Amini, X. Yang, H. Mao, D. L. Rus, S. Han, Bev-fusion: Multi-task multi-sensor fusion with unified bird’s-eye view representation, in: 2023 IEEE international conference on robotics and automation (ICRA), IEEE, 2023, pp. 2774–2781.
<https://doi.org/10.1109/ICRA48891.2023.10160968>
- [15] J. Yin, J. Shen, R. Chen, W. Li, R. Yang, P. Frossard, W. Wang, Is-fusion: Instance-scene collaborative fusion for multimodal 3d object detection, arXiv preprint arXiv:2403.15241 (2024).
<https://doi.org/10.48550/arXiv.2403.15241>
- [16] J. Phillion, S. Fidler, Lift, splat, shoot: Encoding images from arbitrary camera rigs by implicitly unprojecting to 3d, in: Computer Vision–ECCV 2020: 16th European Conference, Glasgow, UK, August 23–28, 2020, Proceedings, Part XIV 16, Springer, 2020, pp. 194–210.
https://doi.org/10.1007/978-3-030-58568-6_12
- [17] Z. Li, W. Wang, H. Li, E. Xie, C. Sima, T. Lu, Y. Qiao, J. Dai, Bev-former: Learning bird’s-eye-view representation from multi-camera images via spatiotemporal transformers, in: European conference on computer vision, Springer, 2022, pp. 1–18.
https://doi.org/10.1007/978-3-031-20077-9_1
- [18] M. Zhang, G. Song, Y. Liu, H. Li, Decoupled detr: Spatially disentangling localization and classification for improved end-to-end object detection, in: Proceedings of the IEEE/CVF International Conference on Computer Vision, 2023, pp. 6601–6610.
<https://doi.org/10.1109/ICCV51070.2023.00607>
- [19] Y. Li, Z. Ge, G. Yu, J. Yang, Z. Wang, Y. Shi, J. Sun, Z. Li, Bevdepth: Acquisition of reliable depth for multi-view 3d object detection, in: Proceedings of the AAAI Conference on Artificial Intelligence, Vol. 37, 2023, pp. 1477–1485.
<https://doi.org/10.1609/aaai.v37i2.25233>

- [20] X. Bai, Z. Hu, X. Zhu, Q. Huang, Y. Chen, H. Fu, C.-L. Tai, Transfusion: Robust lidar-camera fusion for 3d object detection with transformers, in: Proceedings of the IEEE/CVF conference on computer vision and pattern recognition, 2022, pp. 1090–1099.
<https://doi.org/10.1109/CVPR52688.2022.00116>
- [21] J. Huang, G. Huang, Z. Zhu, Y. Ye, D. Du, Bevdet: High-performance multi-camera 3d object detection in bird-eye-view, arXiv preprint arXiv:2112.11790 (2021).
<https://doi.org/10.48550/arXiv.2112.11790>
- [22] J. Hou, Z. Liu, Z. Zou, X. Ye, X. Bai, et al., Query-based temporal fusion with explicit motion for 3d object detection, Advances in Neural Information Processing Systems 36 (2024).
- [23] S. Deng, Z. Liang, L. Sun, K. Jia, Vista: Boosting 3d object detection via dual cross-view spatial attention, in: Proceedings of the IEEE/CVF conference on computer vision and pattern recognition, 2022, pp. 8448–8457.
<https://doi.org/10.1109/CVPR52688.2022.00826>
- [24] H. Caesar, V. Bankiti, A. H. Lang, S. Vora, V. E. Liong, Q. Xu, A. Krishnan, Y. Pan, G. Baldan, O. Beijbom, nuscenes: A multimodal dataset for autonomous driving, in: Proceedings of the IEEE/CVF conference on computer vision and pattern recognition, 2020, pp. 11621–11631.
<https://doi.org/10.1109/CVPR42600.2020.01164>
- [25] J. Huang, Y. Ye, Z. Liang, Y. Shan, D. Du, Detecting as labeling: Rethinking lidar-camera fusion in 3d object detection, arXiv preprint arXiv:2311.07152 (2023).
<https://doi.org/10.48550/arXiv.2311.07152>
- [26] T. Yin, X. Zhou, P. Krahenbuhl, Center-based 3d object detection and tracking, in: Proceedings of the IEEE/CVF conference on computer vision and pattern recognition, 2021, pp. 11784–11793.
<https://doi.org/10.1109/CVPR46437.2021.01161>
- [27] T. Wang, X. Zhu, J. Pang, D. Lin, Fcos3d: Fully convolutional one-stage monocular 3d object detection, in: Proceedings of the IEEE/CVF

- International Conference on Computer Vision, 2021, pp. 913–922.
<https://doi.org/10.1109/ICCVW54120.2021.00107>
- [28] J. Xu, L. Peng, H. Cheng, H. Li, W. Qian, K. Li, W. Wang, D. Cai, Mononerd: Nerf-like representations for monocular 3d object detection, in: Proceedings of the IEEE/CVF International Conference on Computer Vision, 2023, pp. 6814–6824.
<https://doi.org/10.1109/ICCV51070.2023.00627>
- [29] H. Liu, Y. Teng, T. Lu, H. Wang, L. Wang, Sparsebev: High-performance sparse 3d object detection from multi-camera videos, in: Proceedings of the IEEE/CVF International Conference on Computer Vision, 2023, pp. 18580–18590.
<https://doi.org/10.1109/ICCV51070.2023.01703>
- [30] Y. Liu, T. Wang, X. Zhang, J. Sun, Petr: Position embedding transformation for multi-view 3d object detection, in: European Conference on Computer Vision, Springer, 2022, pp. 531–548.
https://doi.org/10.1007/978-3-031-19812-0_31
- [31] S. Wang, Y. Liu, T. Wang, Y. Li, X. Zhang, Exploring object-centric temporal modeling for efficient multi-view 3d object detection, in: Proceedings of the IEEE/CVF International Conference on Computer Vision, 2023, pp. 3621–3631.
<https://doi.org/10.1109/ICCV51070.2023.00335>
- [32] S. Doll, R. Schulz, L. Schneider, V. Benzin, M. Enzweiler, H. P. Lensch, Spatialdetr: Robust scalable transformer-based 3d object detection from multi-view camera images with global cross-sensor attention, in: European Conference on Computer Vision, Springer, 2022, pp. 230–245.
https://doi.org/10.1007/978-3-031-19842-7_14
- [33] A. Vaswani, N. Shazeer, N. Parmar, J. Uszkoreit, L. Jones, A. N. Gomez, Ł. Kaiser, I. Polosukhin, Attention is all you need, *Advances in neural information processing systems* 30 (2017).
<https://doi.org/10.48550/arXiv.1706.03762>
- [34] N. Carion, F. Massa, G. Synnaeve, N. Usunier, A. Kirillov, S. Zagoruyko, End-to-end object detection with transformers, in: European conference

on computer vision, Springer, 2020, pp. 213–229.
https://doi.org/10.1007/978-3-030-58452-8_13

- [35] Z. Li, Z. Yu, W. Wang, A. Anandkumar, T. Lu, J. M. Alvarez, Fb-bev: Bev representation from forward-backward view transformations, in: Proceedings of the IEEE/CVF International Conference on Computer Vision, 2023, pp. 6919–6928.
<https://doi.org/10.1109/ICCV51070.2023.00637>
- [36] Z. Li, F. Wang, N. Wang, Lidar r-cnn: An efficient and universal 3d object detector, in: Proceedings of the IEEE/CVF Conference on Computer Vision and Pattern Recognition, 2021, pp. 7546–7555.
<https://doi.org/10.1109/CVPR46437.2021.00746>
- [37] C. R. Qi, H. Su, K. Mo, L. J. Guibas, Pointnet: Deep learning on point sets for 3d classification and segmentation, in: Proceedings of the IEEE conference on computer vision and pattern recognition, 2017, pp. 652–660.
<https://doi.org/10.1109/CVPR.2017.16>
- [38] C. R. Qi, L. Yi, H. Su, L. J. Guibas, Pointnet++: Deep hierarchical feature learning on point sets in a metric space, Advances in neural information processing systems 30 (2017).
<https://doi.org/10.48550/arXiv.1706.02413>
- [39] S. Shi, X. Wang, H. Li, Pointrcnn: 3d object proposal generation and detection from point cloud, in: Proceedings of the IEEE/CVF conference on computer vision and pattern recognition, 2019, pp. 770–779.
<https://doi.org/10.1109/CVPR.2019.00086>
- [40] C. R. Qi, W. Liu, C. Wu, H. Su, L. J. Guibas, Frustum pointnets for 3d object detection from rgb-d data, in: Proceedings of the IEEE conference on computer vision and pattern recognition, 2018, pp. 918–927.
<https://doi.org/10.1109/CVPR.2018.00102>
- [41] Y. Chen, Y. Li, X. Zhang, J. Sun, J. Jia, Focal sparse convolutional networks for 3d object detection, in: Proceedings of the IEEE/CVF Conference on Computer Vision and Pattern Recognition, 2022, pp. 5428–5437.
<https://doi.org/10.1109/CVPR52688.2022.00535>

- [42] Y. Chen, J. Liu, X. Zhang, X. Qi, J. Jia, Largekernel3d: Scaling up kernels in 3d sparse cnns, in: Proceedings of the IEEE/CVF Conference on Computer Vision and Pattern Recognition, 2023, pp. 13488–13498.
<https://doi.org/10.1109/CVPR52729.2023.01296>
- [43] Y. Zhou, O. Tuzel, Voxelnet: End-to-end learning for point cloud based 3d object detection, in: Proceedings of the IEEE conference on computer vision and pattern recognition, 2018, pp. 4490–4499.
<https://doi.org/10.1109/CVPR.2018.00472>
- [44] Y. Yan, Y. Mao, B. Li, Second: Sparsely embedded convolutional detection, *Sensors* 18 (10) (2018) 3337.
<https://doi.org/10.3390/s18103337>
- [45] J. Li, C. Luo, X. Yang, Pillarnext: Rethinking network designs for 3d object detection in lidar point clouds, in: Proceedings of the IEEE/CVF Conference on Computer Vision and Pattern Recognition, 2023, pp. 17567–17576.
<https://doi.org/10.1109/CVPR52729.2023.01685>
- [46] A. H. Lang, S. Vora, H. Caesar, L. Zhou, J. Yang, O. Beijbom, Pointpillars: Fast encoders for object detection from point clouds, in: Proceedings of the IEEE/CVF conference on computer vision and pattern recognition, 2019, pp. 12697–12705.
<https://doi.org/10.1109/CVPR.2019.01298>
- [47] L. Fan, X. Xiong, F. Wang, N. Wang, Z. Zhang, Rangedet: In defense of range view for lidar-based 3d object detection, in: Proceedings of the IEEE/CVF international conference on computer vision, 2021, pp. 2918–2927.
<https://doi.org/10.1109/ICCV48922.2021.00291>
- [48] J. Bi, H. Wei, G. Zhang, K. Yang, Z. Song, Dyfusion: Cross-attention 3d object detection with dynamic fusion, *IEEE Latin America Transactions* 22 (2) (2024) 106–112.
<https://doi.org/10.1109/TLA.2024.10412035>
- [49] Z. Song, G. Zhang, J. Xie, L. Liu, C. Jia, S. Xu, Z. Wang, Voxelnexthfusion: A simple, unified and effective voxel fusion framework for multi-modal 3d object detection, arXiv preprint arXiv:2401.02702 (2024).
<https://doi.org/10.1109/TGRS.2023.3331893>

- [50] S. Xu, D. Zhou, J. Fang, J. Yin, Z. Bin, L. Zhang, Fusionpainting: Multimodal fusion with adaptive attention for 3d object detection, in: 2021 IEEE International Intelligent Transportation Systems Conference (ITSC), IEEE, 2021, pp. 3047–3054.
<https://doi.org/10.1109/ITSC48978.2021.9564951>
- [51] S. Vora, A. H. Lang, B. Helou, O. Beijbom, Pointpainting: Sequential fusion for 3d object detection, in: Proceedings of the IEEE/CVF conference on computer vision and pattern recognition, 2020, pp. 4604–4612.
<https://doi.org/10.1109/CVPR42600.2020.00466>
- [52] T. Yin, X. Zhou, P. Krähenbühl, Multimodal virtual point 3d detection, Advances in Neural Information Processing Systems 34 (2021) 16494–16507.
<https://doi.org/10.48550/arXiv.2111.06881>
- [53] V. A. Sindagi, Y. Zhou, O. Tuzel, Mvx-net: Multimodal voxelnet for 3d object detection, in: 2019 International Conference on Robotics and Automation (ICRA), IEEE, 2019, pp. 7276–7282.
<https://doi.org/10.1109/ICRA.2019.8794195>
- [54] Z. Chen, Z. Li, S. Zhang, L. Fang, Q. Jiang, F. Zhao, Deformable feature aggregation for dynamic multi-modal 3d object detection, in: European conference on computer vision, Springer, 2022, pp. 628–644.
https://doi.org/10.1007/978-3-031-20074-8_36
- [55] Z. Yang, J. Chen, Z. Miao, W. Li, X. Zhu, L. Zhang, Deepinteraction: 3d object detection via modality interaction, Advances in Neural Information Processing Systems 35 (2022) 1992–2005.
<https://doi.org/10.48550/arXiv.2208.11112>
- [56] T. Liang, H. Xie, K. Yu, Z. Xia, Z. Lin, Y. Wang, T. Tang, B. Wang, Z. Tang, Bevfusion: A simple and robust lidar-camera fusion framework, Advances in Neural Information Processing Systems 35 (2022) 10421–10434.
<https://doi.org/10.48550/arXiv.2205.13790>
- [57] Y. Xie, C. Xu, M.-J. Rakotosaona, P. Rim, F. Tombari, K. Keutzer, M. Tomizuka, W. Zhan, Sparsefusion: Fusing multi-modal sparse representations for multi-sensor 3d object detection, in: Proceedings of the

- IEEE/CVF International Conference on Computer Vision, 2023, pp. 17591–17602.
<https://doi.org/10.1109/ICCV51070.2023.01613>
- [58] J. Yan, Y. Liu, J. Sun, F. Jia, S. Li, T. Wang, X. Zhang, Cross modal transformer: Towards fast and robust 3d object detection, in: Proceedings of the IEEE/CVF International Conference on Computer Vision, 2023, pp. 18268–18278.
<https://doi.org/10.1109/ICCV51070.2023.01675>
- [59] H. Wang, H. Tang, S. Shi, A. Li, Z. Li, B. Schiele, L. Wang, Unitr: A unified and efficient multi-modal transformer for bird’s-eye-view representation, in: Proceedings of the IEEE/CVF International Conference on Computer Vision, 2023, pp. 6792–6802.
<https://doi.org/10.1109/ICCV51070.2023.00625>
- [60] Z. Song, L. Yang, S. Xu, L. Liu, D. Xu, C. Jia, F. Jia, L. Wang, Graphbev: Towards robust bev feature alignment for multi-modal 3d object detection, arXiv preprint arXiv:2403.11848 (2024).
<https://doi.org/10.48550/arXiv.2403.11848>
- [61] J. Zhuang, Z. Qin, H. Yu, X. Chen, Task-specific context decoupling for object detection, arXiv preprint arXiv:2303.01047 (2023).
<https://doi.org/10.48550/arXiv.2303.01047>
- [62] Z. Song, L. Liu, F. Jia, Y. Luo, C. Jia, G. Zhang, L. Yang, L. Wang, Robustness-aware 3d object detection in autonomous driving: A review and outlook, IEEE Transactions on Intelligent Transportation Systems (2024).
<https://doi.org/10.1109/TITS.2024.3439557>
- [63] L. Wang, X. Zhang, Z. Song, J. Bi, G. Zhang, H. Wei, L. Tang, L. Yang, J. Li, C. Jia, et al., Multi-modal 3d object detection in autonomous driving: A survey and taxonomy, IEEE Transactions on Intelligent Vehicles 8 (7) (2023) 3781–3798.
<https://doi.org/10.1109/TIV.2023.3264658>
- [64] Z. Song, H. Wei, L. Bai, L. Yang, C. Jia, Graphalign: Enhancing accurate feature alignment by graph matching for multi-modal 3d object detection, in: Proceedings of the IEEE/CVF International Conference

- on Computer Vision, 2023, pp. 3358–3369.
<https://doi.org/10.1109/ICCV51070.2023.00311>
- [65] Z. Song, C. Jia, L. Yang, H. Wei, L. Liu, Graphalign++: An accurate feature alignment by graph matching for multi-modal 3d object detection, *IEEE Transactions on Circuits and Systems for Video Technology* (2023).
<https://doi.org/10.1109/TCSVT.2023.3306361>
- [66] Z. Chen, Z. Li, S. Zhang, L. Fang, Q. Jiang, F. Zhao, B. Zhou, H. Zhao, Autoalign: pixel-instance feature aggregation for multi-modal 3d object detection, *arXiv preprint arXiv:2201.06493* (2022).
<https://doi.org/10.24963/ijcai.2022/116>
- [67] Z. Song, F. Jia, H. Pan, Y. Luo, C. Jia, G. Zhang, L. Liu, Y. Ji, L. Yang, L. Wang, Contrastalign: Toward robust bev feature alignment via contrastive learning for multi-modal 3d object detection, *arXiv preprint arXiv:2405.16873* (2024).
<https://doi.org/10.48550/arXiv.2405.16873>
- [68] H. Li, H. Zhang, Z. Zeng, S. Liu, F. Li, T. Ren, L. Zhang, Dfa3d: 3d deformable attention for 2d-to-3d feature lifting, in: *Proceedings of the IEEE/CVF International Conference on Computer Vision*, 2023, pp. 6684–6693.
<https://doi.org/10.1109/ICCV51070.2023.00615>
- [69] Y. Chen, J. Liu, X. Zhang, X. Qi, J. Jia, Voxelnext: Fully sparse voxelnet for 3d object detection and tracking, in: *Proceedings of the IEEE/CVF Conference on Computer Vision and Pattern Recognition*, 2023, pp. 21674–21683.
<https://doi.org/10.1109/CVPR52729.2023.02076>
- [70] G. Zhang, C. Junnan, G. Gao, J. Li, X. Hu, Hednet: A hierarchical encoder-decoder network for 3d object detection in point clouds, *Advances in Neural Information Processing Systems* 36 (2024).
<https://doi.org/10.1109/CVPR42600.2020.00047>
- [71] Y. Chen, Z. Yu, Y. Chen, S. Lan, A. Anandkumar, J. Jia, J. M. Alvarez, Focalformer3d: focusing on hard instance for 3d object detection, in: *Proceedings of the IEEE/CVF International Conference on Computer*

- Vision, 2023, pp. 8394–8405.
<https://doi.org/10.1109/ICCV51070.2023.00771>
- [72] H. Wang, C. Shi, S. Shi, M. Lei, S. Wang, D. He, B. Schiele, L. Wang, Dsvt: Dynamic sparse voxel transformer with rotated sets, in: Proceedings of the IEEE/CVF Conference on Computer Vision and Pattern Recognition, 2023, pp. 13520–13529.
<https://doi.org/10.1109/CVPR52729.2023.01299>
- [73] Z. Liu, J. Hou, X. Wang, X. Ye, J. Wang, H. Zhao, X. Bai, Lion: Linear group rnn for 3d object detection in point clouds, arXiv preprint arXiv:2407.18232 (2024).
<https://doi.org/10.48550/arXiv.2407.18232>
- [74] Y. Li, Y. Chen, X. Qi, Z. Li, J. Sun, J. Jia, Unifying voxel-based representation with transformer for 3d object detection, Advances in Neural Information Processing Systems 35 (2022) 18442–18455.
<https://doi.org/10.48550/arXiv.2206.00630>
- [75] Q. Cai, Y. Pan, T. Yao, C.-W. Ngo, T. Mei, Objectfusion: Multi-modal 3d object detection with object-centric fusion, in: Proceedings of the IEEE/CVF International Conference on Computer Vision, 2023, pp. 18067–18076.
<https://doi.org/10.1109/ICCV51070.2023.01656>
- [76] Y. Jiao, Z. Jie, S. Chen, J. Chen, L. Ma, Y.-G. Jiang, Msmdfusion: Fusing lidar and camera at multiple scales with multi-depth seeds for 3d object detection, in: Proceedings of the IEEE/CVF Conference on Computer Vision and Pattern Recognition, 2023, pp. 21643–21652.
<https://doi.org/10.1109/CVPR52729.2023.02073>
- [77] M. Contributors, MMDetection3D: OpenMMLab next-generation platform for general 3D object detection, <https://github.com/open-mmlab/mmdetection3d> (2020).
- [78] Z. Liu, Y. Lin, Y. Cao, H. Hu, Y. Wei, Z. Zhang, S. Lin, B. Guo, Swin transformer: Hierarchical vision transformer using shifted windows, in: Proceedings of the IEEE/CVF international conference on computer vision, 2021, pp. 10012–10022.
<https://doi.org/10.1109/ICCV48922.2021.00986>

- [79] B. Zhu, Z. Jiang, X. Zhou, Z. Li, G. Yu, Class-balanced grouping and sampling for point cloud 3d object detection, arXiv preprint arXiv:1908.09492 (2019).
<https://doi.org/10.48550/arXiv.1908.09492>
- [80] K. He, X. Zhang, S. Ren, J. Sun, Deep residual learning for image recognition, in: Proceedings of the IEEE conference on computer vision and pattern recognition, 2016, pp. 770–778.
<https://doi.org/10.1109/CVPR.2016.90>
- [81] Y. Lee, J. Park, Centermask: Real-time anchor-free instance segmentation, in: Proceedings of the IEEE/CVF conference on computer vision and pattern recognition, 2020, pp. 13906–13915.
<https://doi.org/10.1109/CVPR42600.2020.01392>
- [82] Y. Dong, C. Kang, J. Zhang, Z. Zhu, Y. Wang, X. Yang, H. Su, X. Wei, J. Zhu, Benchmarking robustness of 3d object detection to common corruptions, in: Proceedings of the IEEE/CVF Conference on Computer Vision and Pattern Recognition, 2023, pp. 1022–1032.
<https://doi.org/10.1109/CVPR52729.2023.00105>